# Rapid determination of local composition in quasi-binary, inhomogeneous material systems from backscattered electron image contrast

**Mohammad Yasseri*[,a,b], Nader Farahi[b], Klemens Kelm[b], Eckhard Mueller[a,b], Johannes de Boor*[,b]**

[a]Institute of Inorganic and Analytical Chemistry, Justus-Liebig University Giessen, D – 35392 Giessen, Germany.

[b]Institute of Materials Research, Linder Hoehe, German Aerospace Center (DLR), D – 51147 Koeln, Germany.

Corresponding Author(s): Mohammad Yasseri@dlr.de, Johannes.deBoor@dlr.de

**Abstract**

Quantification of different phases in multiphase materials and the determination of compositions in material systems with extended solubility of the components are crucial for the engineering of material properties. In the field of thermoelectrics, multiphase materials are of considerable interest due to the additional scattering caused by different phases, reducing the lattice thermal conductivity and consequently improving the thermoelectric performance of the material. Size, shape, amount, and composition of secondary phases need to be assessed and optimized to be able to tune the material properties. SEM-EDX is the state-of-the-art method for such phase analysis. It suffers, however, from a low throughput and a limited

spatial resolution. In this work, we demonstrate a simple relation between the grey value in backscattered electron images and the chemical composition allowing for a rapid method for phase quantification (with respect to composition as well as compositional fraction) in quasi-binary multiphase or wide solubility material systems. Applying this method to $Mg_2Si_xSn_{1-x}$, the Si and Sn content of each individual point on the BSE images can be calculated. The introduced SEM image analysis is much faster compared to EDX mapping as it requires only two EDX point measurements for calibration. Moreover, it also provides a superior spatial resolution.

**Keywords:** phase quantification, quasi-binary multiphase materials, thermoelectric, magnesium silicide stannide, backscattered electron image

## 1- Introduction

Multiphase materials are very common in materials science and technology and are often dealt with in a wide variety of applications, such as superalloys [1, 2], shape memory alloys [3], multiphase steels [4], thermoelectrics [5], etc. Thermoelectric materials are ranked according to their thermoelectric figure of merit $zT$ which is given by a combination of material properties $zT = \frac{\sigma S^2}{\kappa} T$ [6]. Here $S$ is the Seebeck coefficient, $\sigma$ the electrical conductivity and $\kappa$ the thermal conductivity which comprises of electronic, bipolar, and lattice contributions. Multiphase materials can show additional phonon scattering and, consequently, a lower lattice thermal conductivity compared to single phase materials [7, 8]. Therefore, reduction in thermal conductivity due to the presence of secondary phases in forms of nanoinclusions and compositional inhomogeneities results in a greater $zT$ provided that the detrimental influence of such structures on the electronic performance is minor [9, 10]. This strategy was realized for PbTe based alloys like LAST-$m$ (lead antimony silver telluride ($AgPb_mSbTe_{2+m}$)) where first it was shown that phase segregation leads to an improved

thermoelectric performance and second that the extend of the improvement depends on the size of the secondary phases as well as their distribution in the matrix [5, 11]. Another parameter which influences the effect of the secondary phases on the scattering of acoustic phonons, and consequently, the reduction of the thermal conductivity is the coherency of the secondary phases to the matrix. If the coherency is high, the scattering of charge carriers at an interface and, thereby the deterioration of the electronic performance is minor [12]. Thus, the difference between the chemical composition of the secondary phases and the matrix, influencing the lattice parameter mismatch, the chemical bonding at the interface as well as the match between electronic and phononic band structure influences the overall thermoelectric properties of the composite. Secondary phases can also be beneficial in heterostructures for blocking undesired minority carriers and hence suppressing the bipolar part of the thermal conductivity or filtering the low energy majority carriers (energy filtering), therefore enhancing the power factor ($\mathrm{PF} = \sigma S^2$) [8, 13]. To sum up, the size, amount, and the composition of the secondary phases should be engineered for improving the properties of any multiphase thermoelectric material.

Apart from the LAST alloys, $Mg_2Si_xSn_{1-x}$ solid solutions have also shown a high potential for thermoelectric applications giving high $zT_{max}$ values of ~1.1–1.4 for n-type $Mg_2Si_{0.4}Sn_{0.6}$ solid solutions [14, 15] and also showing progress for the p-type [16]. There is a miscibility gap reported in the phase diagram of the $Mg_2$(Si,Sn) quasi-binary material system, where a separation of the phases takes place [17, 18]. It is also clear that the phase separation in $Mg_2Si_xSn_{1-x}$ is temperature dependent, though the reported results on the range of the miscibility gap are disputed and contradicting (e.g. $0.4 < x < 0.6$ and $0.34 < x < 0.92$ at room temperature) [17, 19]. In most of the previous reports a composition of $Mg_2Si_{0.5}Sn_{0.5}$ is supposed to be within the miscibility gap [17, 19]. Synthesis of this composition might thus lead to the formation of a multiphase material which makes it an ideal candidate to study the interplay between synthesis parameters, amount and distribution of phases and local chemical

compositions, as well as the resulting thermoelectric properties. To be able to do so, an efficient rapid method for quantification phases and local compositions is indispensable.

Quantification of different phases has been done for decades by different metallography methods such as light optical microscopy via dark-field illumination [20]. There are a number of software developed for this task e.g. image analyzer [21]. Tartaglia et al. [22] have also reported the area percentage of different phases in Mg-Alloys using an automated optical image analyzer. However, there is no systematic method reported for such quantification for scanning electron microscopy (SEM) images which provides a much better spatial resolution.

In addition, determining the compositions of the secondary phases as well as the matrix is crucial for multiphase materials which cannot be provided by optical microscopy. Therefore, there is a high demand for SEM and energy-dispersive X-ray spectroscopy (EDX) as the commonly used method for such phase identification. Depending on excitation energy of elements and accelerating voltage, EDX elemental/ compositional mapping can be very time consuming for conventional EDX systems (e.g. 4h for a 2500 $\mu m^2$ region of $Mg_2(Si,Sn)$), slowing down research progress. Furthermore, obtaining a satisfactory spatial resolution using EDX, necessary for fine structures, can be challenging. Transmission electron microscopy (TEM)-EDX, on the other hand can provide excellent spatial resolution but can only be performed with a drastically lower (areal) throughput than SEM-EDX. Thus, development of a quick and simple method for phase quantification (in composition and volume fraction) is highly desired. A step in that direction was taken by Vajda et al. who quantified the mineral content in bone and found a roughly linear relationship between EDX-determined wt.% Ca and the grey values of backscattered electron (BSE) images of bone mineral (specifically $[Ca_{10}(PO_4)_6(OH)_2]$) [23].

The objective of the present study was to develop a facile method for the quantification of quasi-binary material systems based on image contrast (grey value), using $Mg_2Si_xSn_{1-x}$ as a well-fitting example. In this work, we considered the grey value of the BSE images as a scale

for the amount of the silicon content in the different compositions. The essential idea was to find a mathematical correlation between the grey value of the pixels of the BSE images and the composition of the $Mg_2(Si,Sn)$ compounds (as a quasi-binary system) so that one can use the grey value instead of EDX results to obtain the chemical composition at any position of the BSE image. The BSE coefficient (Ƞ) is the link between the grey values of the BSE images and the chemical composition of the samples. Ƞ is defined as a fraction of incident electrons that reappears as back scatter electrons, which is governed dominantly by the atomic number of elements, and has little dependency on probe current or accelerating voltage [24-26]. For elements heavier than Neon ($Z \geq 10$) Ƞ relates to the atomic number approximately as follows (1);

$$\eta = \frac{\ln Z}{6} - \frac{1}{4} \quad (1);$$

where $Z$ is the atomic number of the element of interest [24]. Notice that the atomic numbers of the elements Mg (12), Si (14), and Sn (50) are well within the applicability range of the Formula (1). Favorably, most of common TE materials such as silicides, PbTe, half-Heusler, Skutterudites, etc. are made of elements which are well within the applicability range of the Formula (1), as they do not contain light elements.

The weighted mean BSE coefficient of complex compositions can be calculated using the Formula (2);

$$\bar{\eta} = \sum_{i=0}^{n} C_i \ \eta_i \quad (2);$$

where $C_i$ and $\eta_i$ are the weight fraction and the BSE coefficient of the element $i$, respectively [24].

## 2- Experiment and methods

Magnesium tin silicide samples with a composition of $Mg_2(Si,Sn,Sb)$ were synthesized by high energy ball milling of the elements (12 h) followed by a compaction step as described in [15]. As the effect on $\bar{\Pi}$ is very small, Sb was disregarded in the following calculations. The samples were sintered at 700 ˚C with different time durations of 20, 60, 120, and 300 minutes to investigate the stability of the Si- rich compositions in the compounds as well as the homogeneity of the samples. The relative densities of the sintered samples were obtained to be >95% of the theoretical value (2.9 $g.cm^{-3}$), using Archimedes' method. It indicates that there is no severe porosity in the samples. Furthermore, the samples were mechanically stable and we did not see any crack on the surface areas of the samples, where the measurements were done. The samples were ground with SiC grinding papers starting with Grit 1200, and continuing with Grit 2500 and Grit 4000 leading to a good surface quality. Back scattered electron images were taken using a Zeiss Ultra 55 SEM with a Zeiss QBSE detector, also equipped with an Oxford energy dispersive X-ray (EDX) detector (PentaFETx3).

To identify the average grey values of areas of interest, the software Fiji, which is a distribution of the popular Open Source software ImageJ, was utilized.

## 3- Results

Figure 1.a shows a typical BSE SEM image of an $Mg_2Si_{0.5}Sn_{0.5}$ sample sintered at 700 ˚C for 20 minutes. The spots measured by EDX are indicated with red crosses. The obtained chemical compositions of the measured spots are listed in Table 1 (see also Figure S1 and Table S1). According to the table, Mg is basically constant while Si:Sn varies in a relatively wide range. To calculate the BSE coefficient, the weight fraction of each element was calculated using Formula (3);

$$C_i=\frac{M_i n_i}{\sum_{i=1}^{n} M_i n_i} \quad (3);$$

where $n_i$, $C_i$, and $M_i$ are atomic fraction, weight fraction, and atomic mass of the element *i*, respectively. The corresponding BSE coefficient of each spot was then calculated using Formula (1) and (2). As the BSE coefficient of each point is calculated from the weight fraction of the elements, which is obtained by EDX, the error for the BSE coefficient is similar to the systematic error of EDX setup.

The X-ray spatial resolution depends on the material density and the accelerating voltage [27] and it can be estimated using Formula (4);

$$R = 0.064 (E_0^{1.68} - E_C^{1.68})/\rho \qquad (4)$$

where R is spatial resolution in μm, $E_o$ is accelerating voltage in keV, $E_c$ is critical excitation energy in keV; and ρ is the mean specimen density in g/cm$^{-3}$. In this EDX measurement the accelerating voltage of 15 kV was employed to get the optimized counts per second (cps) and spatial resolution. As the critical excitation energy of a compound is determined by its heaviest element, the critical excitation energy for $Mg_2Si_{0.5}Sn_{0.5}$ was estimated to be $E_c = 3.44$ keV [28], which is related to Sn as the heaviest element included in this compound.

The grey values corresponding to the EDX measurement spots were obtained by averaging over the pixel grey values (Table 1) in an area corresponding to the EDX spatial resolution, see Figure 1b.

**Table 1: Spectrum number, chemical composition, calculated BSE coefficient ($\bar{\eta}$), and grey value of the EDX point analysis.**

| Spectrum no. | Mg (at. %) | Si (at. %) | Sn (at. %) | $\bar{\eta}$ | Grey value |
|---|---|---|---|---|---|
| 1 | 66.78 | 33.18 | 0.04 | 0.174 | 5.372 |
| 2 | 66.42 | 26.17 | 7.41 | 0.235 | 105.5 |
| 3 | 66.72 | 20.49 | 12.79 | 0.265 | 156.1 |
| 4 | 66.39 | 25.35 | 8.26 | 0.240 | 120.0 |

| | | | | | |
|---|---|---|---|---|---|
| 5 | 66.28 | 14.50 | 19.21 | 0.293 | 213.3 |
| 6 | 66.16 | 14.97 | 18.87 | 0.291 | 206.1 |
| 7 | 66.32 | 24.59 | 9.09 | 0.245 | 122.7 |
| 8 | 66.61 | 33.17 | 0.22 | 0.176 | 8.020 |
| 9 | 66.72 | 27.65 | 5.63 | 0.222 | 89.61 |
| 10 | 66.74 | 32.51 | 0.75 | 0.181 | 5.183 |

If we assume that the difference between the grey values of the points in the image is mainly determined by the difference in the BSE coefficient ($\bar{\eta}$), and $\bar{\eta}$ has a direct correlation with the grey value, the grey value of a pixel in any image is given by *grey value* = $A \times \bar{\eta} + B$ (with *A* and *B* related to contrast and image brightness [23]). In Figure 2, the BSE coefficient is plotted versus grey value using the numbers from Table 1.

As it is shown in Figure 2, the BSE coefficient varies linearly with the grey value exhibiting a regression line ($R^2 = 0.9962$), indicating plausibility of the chosen approach. In this case we could demonstrate that the grey value varies linearly with $\bar{\eta}$ irrespective of the values of A and B. Note that the fit has been obtained over a relatively broad compositional range with $43.3 < x < 99.5$. This shows that the BSE coefficient of any arbitrary point of the image can be obtained with good accuracy after a BSE vs. grey value calibration; this requires only two points in the image as the relation is linear. Next, the chemical composition of any point can be calculated from its corresponding BSE coefficient. For $Mg_ySi_xSn_z$ we have in principle 3 unknowns ($n_{Si}$, $n_{Sn}$, $n_{Mg}$), however the Mg content is fixed around 0.66 (see Table 1) and magnesium silicide stannide is basically a daltonide compound and thus $n_{Mg} + n_{Si} + n_{Sn} = 1$. In consequence the system has effectively only one degree of freedom (Si to Sn ratio).

Employing Equation (2) and (3) $\bar{\eta}$ can be expressed as;

$$\bar{\eta} = \frac{n_{Mg} M_{Mg} \eta_{Mg} + n_{Si} M_{Si} \eta_{Si} + (1-n_{Mg}-n_{Si}) M_{Sn} \eta_{Sn}}{n_{Si} M_{Si} + n_{Mg} M_{Mg} + (1-n_{Mg}-n_{Si}) M_{Sn}},$$

which can be rewritten to obtain e.g. $n_{Si}$:

$$n_{Si} = \frac{\bar{\eta}\left(-n_{Mg} M_{Mg} - (1-n_{Mg}) M_{Sn}\right) + n_{Mg} \eta_{Mg} M_{Mg} + (1-n_{Mg}) \eta_{Sn} M_{Sn}}{\bar{\eta}\left(M_{Si} - M_{Sn}\right) - M_{Si} \eta_{Si} + M_{Sn} \eta_{Sn}} \qquad (5)$$

Equation (5) can then be employed to calculate $n_{Si}$ for the complete SEM BSE image; similarly $n_{Sn}$ can be obtained. Figure 3 shows an example of such mapping for the same sample as shown in Figure 1. To estimate the uncertainty range, we compared the calculated Si content with the measured Si content by EDX, at the points where we did the calibration (the data points in Fig. 2). The average relative uncertainty of the obtained composition was around 0.6%.

Knowledge of the Si content of the image pixels allows for a detailed analysis of the occurring compositions and a straightforward quantification. Figure 4a shows a captured BSE image from a sample sintered at 700 ˚C for 20 minutes and its chemical composition map (Figure 4b). The distribution histogram of the Si contents of the image pixels is plotted in Figure 4c. According to this histogram, the $Mg_2Si_xSn_{1-x}$ composition with $x = 0.475 \pm 0.025$ has the highest number of counts of pixels over the image. The composition of the matrix is thus close to the nominal composition, corresponding to $x$=0.5. Furthermore, if for instance $Mg_2Si_xSn_{1-x}$ compositions with $x \geq 0.6$ are defined as the Si- rich compositions, the cumulative percentage of such compositions can be plotted vs. the Sn molar ratio (1-$x$), as shown in Figure 4d.

Figure 5 shows the area percentage of $Mg_2Si_xSn_{1-x}$ with $x \geq 0.6$ in the samples sintered at 700 ˚C for different time durations. According to this result, the Si-rich compositions decreased with time (i.e. dissolved into the matrix) at 700 ˚C.

## 4- Discussion

### 4-1- Comparison of EDX to the calculated BSE maps with respect to measurement time and spatial resolution

As shown in the results section, if there is a quasi-binary material system which has various phases or a wide solubility range between two end members such as $Mg_2Si$ and $Mg_2Sn$, it is possible to use the grey value to get the approximate composition at any point without extensive EDX measurements. Only two EDX point measurements are needed to get a calibration making the measuring rate much faster compared with EDX mapping. For EDX mappings, there is a compromise between the rate of the measurements and the obtained spatial resolution. The better the required spatial resolution, the longer the time is needed for EDX measurements. On the other hand, use of higher accelerating voltages and thus higher counts usually results in larger interaction volumes, which consequently decreases the spatial resolution of the X-ray image and increases the analytical volume [26]. Since spatial resolution depends on instrument operating conditions and the material, there is no simple recipe for the lowest acceleration voltage which leads to the best spatial resolution [26, 29, 30]. In our measurement, an acceleration voltage of 8 kV was chosen initially because it is greater than twice the critical excitation energy of Sn (3.44 keV) as recommended e.g. in [31]. Using Equation (4), the corresponding calculated spatial resolution for this measurement is 0.55 µm. Figure 6 shows the EDX mapping of the $Mg_2Si_{0.5}Sn_{0.5}$ sample sintered at 700 ˚C for 20 minutes, where the acceleration voltage was selected to be 8 kV and the measurement was run for 20 minutes. The calculated Si content of the area of interest using Equation (5) is also mapped, see Figure 6e. It is visible that the quality of the quantified map for the Si content (Figure 6e) is much better than the corresponding EDX map (Figure 6d). The reason is that the penetration width and depth of the back scattered electrons in the pear shaped electron distribution volume is smaller than the corresponding depth of the characteristic X-rays [32].

Furthermore, the detected number of the emitted X-rays per time is much lower than the detected back scattered electrons. Therefore, EDX mapping needs a longer time compared with BSE imaging to provide a high quality image and low signal to noise ratio. To improve the total counting statistics of the EDX mapping, the acceleration voltage can be increased. Figure 7 shows an EDX map obtained by employing the acceleration voltage of 25 kV for 40 minutes for the same sample (with a calculated spatial resolution of 4.75 µm, using Formula (4)). Figure 7c and 7d show the EDX map of the Si content and the calculated Si content of the area of interest (using Equation (5)), respectively. The quality (the signal to noise ratio) of the EDX map (Fig. 7d) is apparently better than that of the EDX map in Figure6d, however, the spatial resolution is lower than both the low voltage EDX map (Fig. 6d) and the corresponding calculated BSE map (Fig. 7e). These results indicate that the processing time and the obtained quality of the BSE derived chemical composition maps are superior compared to the EDX maps, for which two different sets of acceleration voltage and time durations were tested. Generally, the BSE spatial resolution is better than that of the EDX [33].

### 4-2- Scope and limitations

In this section we want to discuss the proper use of the presented analysis method and the associated uncertainties. The contrast, brightness, working distance, aperture size, incident electron beam angle, convergence angle, and the acceleration voltage should stay the same during one set of SEM measurements as changing any of these parameters can vary the slope of the linear correlation between grey value and $\overline{\Pi}$ in *grey value* = $A \times \overline{\Pi} + B$, introducing errors and invalidating the assumption of the linearity. For example if the roughness of the specimen surface is high, the incident angle of the electron beam has a tilted penetration pear shape at the sample surface and it influences the BSE coefficient [25, 34]. The method should also be applied only for analysis of the specimens which have a sufficiently high electrical

conductance to avoid any charging effect. In the $Mg_2Si_xSn_{1-x}$ samples, the electrical conductivity is around $10^3$ S/cm and no charging effect was observed. Another issue is the mixed penetration depth of the incident electron beam in the different phases of a sample. EDX corrects the error by its absorption correction factors [27] but BSE imaging data does not include such corrections. In addition, this analysis can include some errors in the case the magnification is very low. The reason is that the electron beam scans different areas of the sample with a different angle of incidence where $\eta$ depends on the angle [25, 34], consequently this leads to a non-linearity of the grey value vs. $\eta$. Different elements show this effect to a different extent [25]. It is therefore difficult to give a general magnification limit, but it is easily possible to establish an empirical limit by the BSE measurements of the pure phases at low magnifications. We found little angular dependence for the investigated systems for horizontal field width (HFW) of about 2000 µm or smaller on our material system. It is worth mentioning that in images with very small HFW (100 µm) where grains are visible, the grey value of the grains might vary from grain to grain with a change in the crystallite orientations, when the composition variation is small over the sample. The so called channeling effect [31] might introduce a small systematic error in the quantification but will not dominate the contrast in the composite $Mg_2(Si,Sn)$ system. Varying the orientation of the grains with respect to the beam either by slightly tilting the sample or tilting the beam (which happens at low magnifications) will make this contrast contribution vanish. The final limitation is that the system needs to be truly quasi-binary, i.e. free of other secondary phases (e.g. MgO in our example) and with constant Mg content. For $Mg_2(Si,Sn)$ [35, 36], however the phase width with respect to Mg content is considered to be so small that is negligible for the performed analysis.

Practically, the influence of the listed limitations can be estimated by checking the linearity between grey value and BSE coefficient. For the results discussed here Figure 2 confirms the

applicability of the suggested analysis method for the $Mg_2Si_xSn_{1-x}$ quasi-binary material system.

## 5- Conclusion

In this study we introduce a rapid method for phase quantification (with respect to composition as well as compositional fraction) in quasi-binary multiphase or wide solubility material systems such as $Mg_2Si_xSn_{1-x}$. We utilize the linearity between the grey value of BSE images and the average BSE coefficient which in turn is related to the chemical composition of the material. Using $Mg_2Si_xSn_{1-x}$ as an example, the Si and Sn content of each individual point on the BSE images could be calculated based on only two EDX point measurements for calibration. Furthermore, we were able to determine the (area) fractions of the different compositional fractions. The proposed chemical composition mapping is found to be superior to EDX mappings with respect to acquisition rate and spatial resolution. The method, therefore, can be used as a strong analysis tool for phase quantification and compositional analysis of quasi-binary material systems.

## Acknowledgments

The authors would like to gratefully acknowledge the endorsement from the DLR Executive Board Member for Space Research and Technology and the financial support from the Young Research Group Leader Program. The authors would also like to thank P. Ponnusamy, H. Kamila, and A. Sankhla (DLR) for their valuable support of the scientific work. Many thanks go to C. Stiewe and R. Sottong (DLR) for their help in sample preparation. M.Y. would like to thank for his financial support which is provided by the DFG via the GRK (Research Training Group) 2204 "Substitute Materials for Sustainable Energy Technologies“. Also, financial support of one of the authors (N.F.) is provided by the DAAD (Fellowship No.: 241/2016).

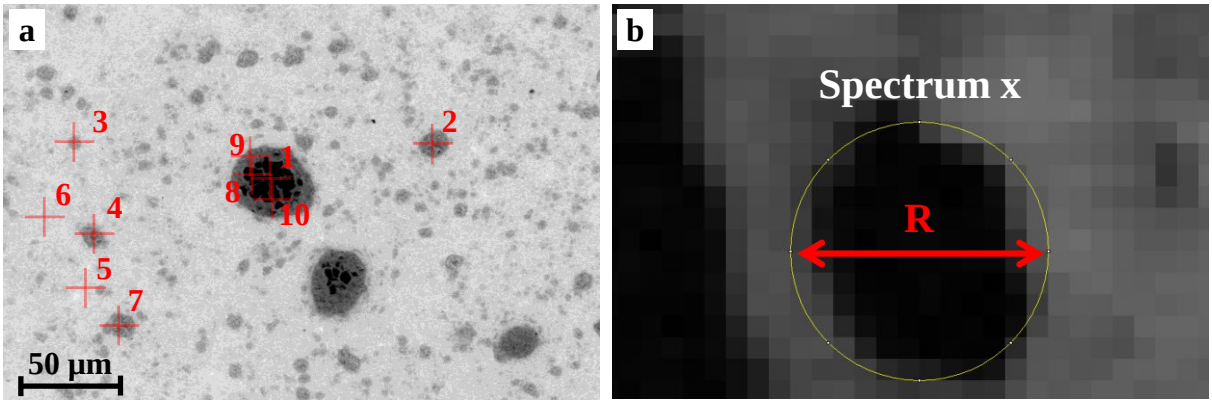


**Figure 1: a) Typical BSE SEM picture of multiphase $Mg_2(Si,Sn)$, b) zoom-in indicating the region used to obtain average of grey scale values around a particular point (spatial resolution (R) was estimated as 2-4 µm and its value was used as the diameter of each spot). The details on phase evolution of $Mg_2(Si,Sn)$ ball-milled powders and sintered samples are discussed in [13].**

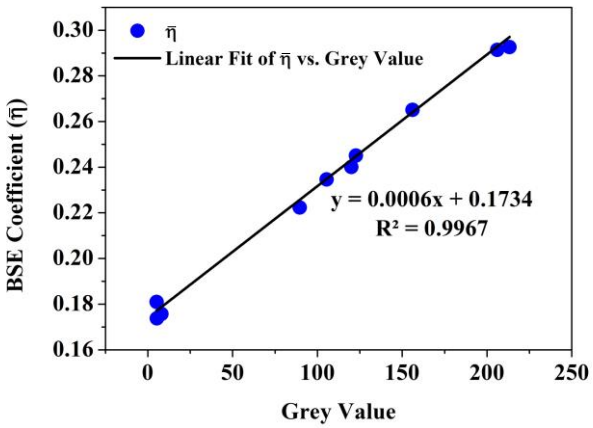


**Figure 2: Grey value vs. BSE coefficient for the BSE image shown in Fig. 1.**

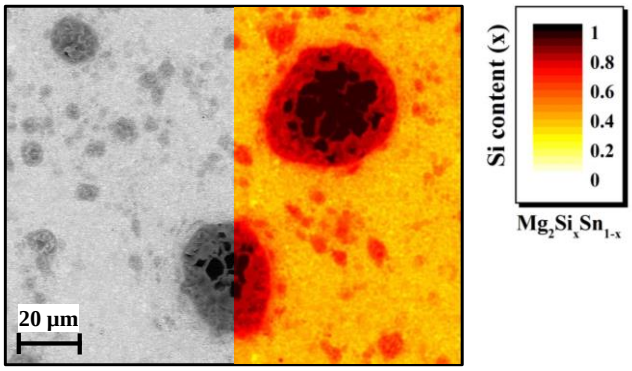


**Figure 3: a) A typical BSE SEM picture of multiphase $Mg_2(Si,Sn)$ together with an overlay of corresponding chemical composition map obtained using Equation (5).**

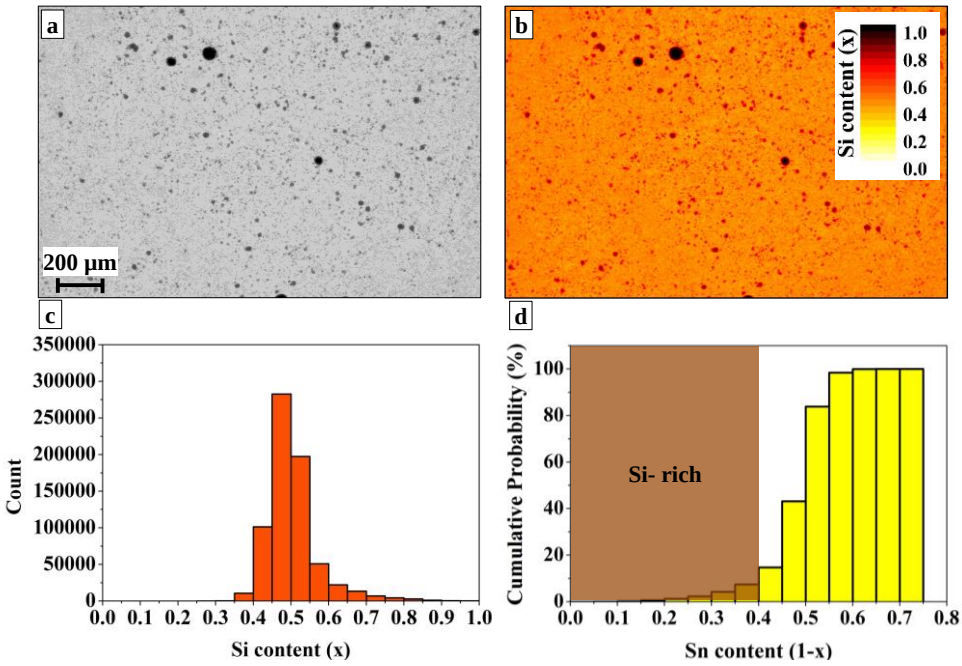


**Figure 4: a) BSE image of an $Mg_2Si_{0.5}Sn_{0.5}$ sample sintered at 700 ˚C for 20 minutes, b) the chemical composition map for the BSE image, c) the distribution histogram of the Si contents in compositions, and d) the cumulative probability diagram of Si-rich compositions.**

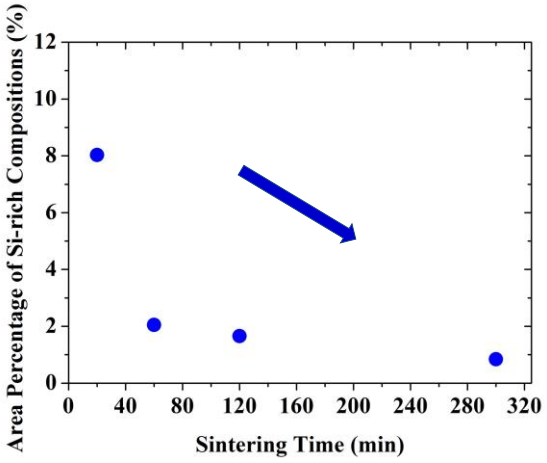


**Figure 5: The area percentage as obtained from Equation (5) of the $Mg_2Si_xSn_{1-x}$ compositions with $x \geq 0.6$ in the samples sintered at 700 ˚C.**

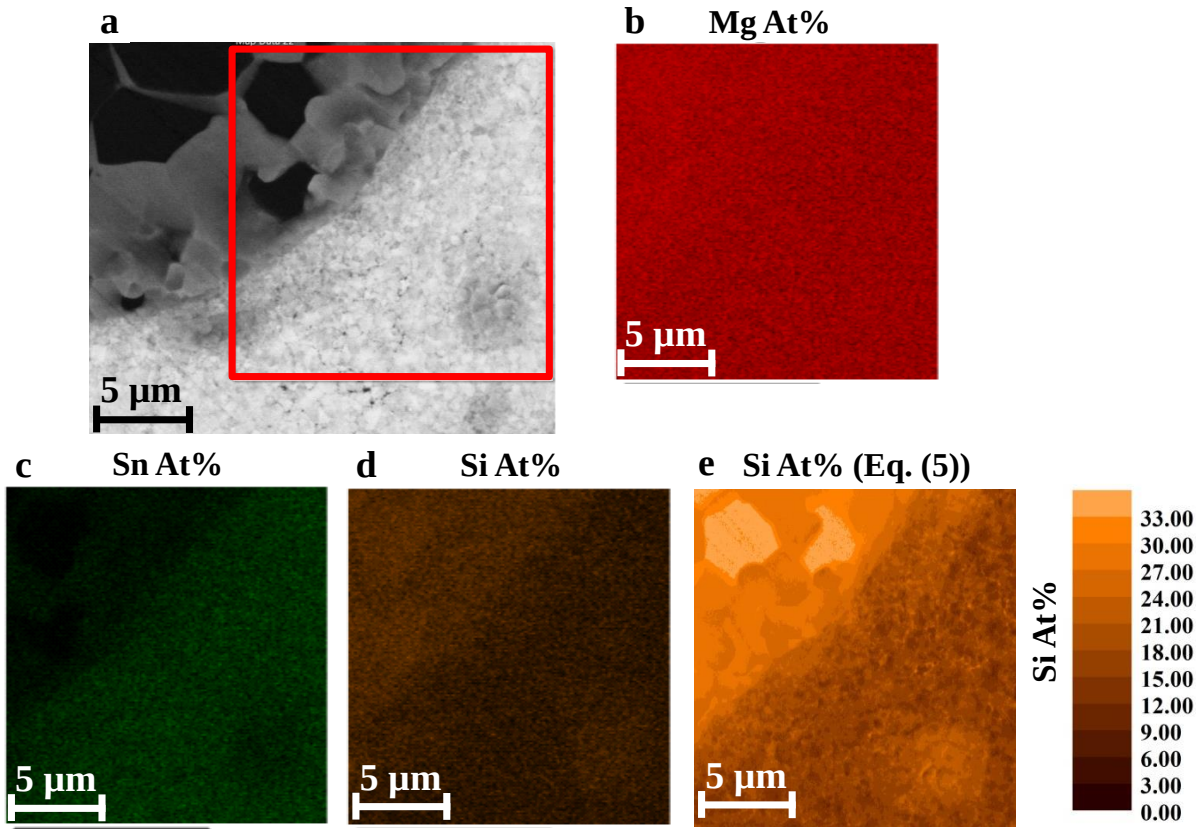


**Figure 6: a) BSE image of the $Mg_2Si_{0.5}Sn_{0.5}$ sample sintered at 700 ˚C for 20 minutes. Figures b, c, and d, show the EDX maps of the elements Mg, Sn, and Si, respectively and Figure e shows the quantified map of the Si content for the area of interest. The EDX mapping was done for 20 minutes with acceleration voltage of 8 kV.**

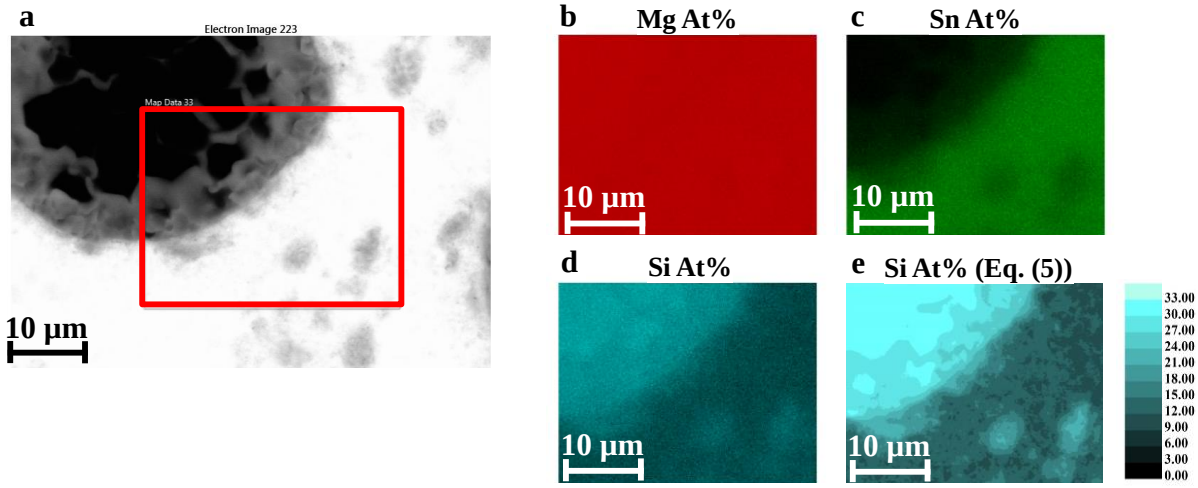


**Figure 7: a) BSE image of the sample sintered at 700 ˚C for 20 minutes. Figures b, c, d, and e show the EDX maps of the elements Mg, Sn, and Si, and the calculated BSE map of the element Si, respectively. The EDX mapping was done for 40 minutes with acceleration voltage of 25 kV.**

## **Appendix A**. **Supplementary data**

Supplementary data related to this article can be found at http:// dx.doi.org/xxx.

## References


[1] K. Shinagawa, H. Chinen, T. Omori, K. Oikawa, I. Ohnuma, K. Ishida, R. Kainuma, Phase equilibria and thermodynamic calculation of the Co–Ta binary system, Intermetallics 49 (2014) 87-97.
[2] M. Krüger, High temperature compression strength and oxidation of a V-9Si-13B alloy, Scripta Materialia 121 (2016) 75-78.
[3] K.V. Ramaiah, C.N. Saikrishna, J. Bhagyaraj, Gouthama, S.K. Bhaumik, Influence of Sc addition on microstructure and transformation behaviour of Ni24.7Ti50.3Pd25.0 high temperature shape memory alloy, Intermetallics 40 (2013) 10-18.
[4] A. Varshney, S. Sangal, Gouthama, A.K. Pramanick, K. Mondal, Microstructural evidence of nano-carbides in medium carbon high silicon multiphase steels, Materials Science and Engineering: A 708 (2017) 237-247.
[5] M.G. Kanatzidis, Nanostructured Thermoelectrics: The New Paradigm?†, Chemistry of Materials 22(3) (2010) 648-659.
[6] G.J. Snyder, E.S. Toberer, Complex thermoelectric materials, Nat Mater 7(2) (2008) 105-14.
[7] A. Yamini, T. Li, D.R.G. Mitchell, J.M. Cairney, Elemental distributions within multiphase quaternary Pb chalcogenide thermoelectric materials determined through three-dimensional atom probe tomography, Nano Energy 26 (2016) 157-163.
[8] L.-D. Zhao, V.P. Dravid, M.G. Kanatzidis, The panoscopic approach to high performance thermoelectrics, Energy Environ. Sci. 7(1) (2014) 251-268.
[9] A. Nozariasbmarz, P. Roy, Z. Zamanipour, J.H. Dycus, M.J. Cabral, J.M. LeBeau, J.S. Krasinski, D. Vashaee, Comparison of thermoelectric properties of nanostructured Mg2Si, FeSi2, SiGe, and nanocomposites of SiGe–Mg2Si, SiGe–FeSi2, APL Materials 4(10) (2016) 104814.
[10] Y. Zhou, X. Gong, B. Xu, M. Hu, First-principles and molecular dynamics study of thermoelectric transport properties of N-type silicon-based superlattice-nanocrystalline heterostructures, Journal of Applied Physics 122(8) (2017) 085105.
[11] B.A. Cook, M.J. Kramer, J.L. Harringa, M.-K. Han, D.-Y. Chung, M.G. Kanatzidis, Analysis of Nanostructuring in High Figure-of-Merit Ag1-xPbmSbTe2+mThermoelectric Materials, Advanced Functional Materials 19(8) (2009) 1254-1259.
[12] S. Perlt, T. Höche, J. Dadda, E. Müller, P. Bauer Pereira, R. Hermann, M. Sarahan, E. Pippel, R. Brydson, Microstructure analyses and thermoelectric properties of Ag1-xPb18Sb1+yTe20, Journal of Solid State Chemistry 193 (2012) 58-63.
[13] J.-H. Bahk, A. Shakouri, Enhancing the thermoelectric figure of merit through the reduction of bipolar thermal conductivity with heterostructure barriers, Applied Physics Letters 105(5) (2014) 052106.
[14] W. Liu, X. Tan, K. Yin, H. Liu, X. Tang, J. Shi, Q. Zhang, C. Uher, Convergence of conduction bands as a means of enhancing thermoelectric performance of n-type Mg2Si(1-x)Sn(x) solid solutions, Phys Rev Lett 108(16) (2012) 166601.
[15] A. Sankhla, A. Patil, H. Kamila, M. Yasseri, N. Farahi, E. Mueller, J. de Boor, Mechanical Alloying of Optimized Mg2(Si,Sn) Solid Solutions: Understanding Phase Evolution and Tuning Synthesis Parameters for Thermoelectric Applications, ACS Applied Energy Materials 1(2) (2018) 531-542.
[16] J. de Boor, T. Dasgupta, U. Saparamadu, E. Müller, Z.F. Ren, Recent progress in p-type thermoelectric magnesium silicide based solid solutions, Materials Today Energy 4 (2017) 105-121.
[17] A. Kozlov, J. Gröbner, R. Schmid-Fetzer, Phase formation in Mg–Sn–Si and Mg–Sn–Si–Ca alloys, Journal of Alloys and Compounds 509(7) (2011) 3326-3337.
[18] R. Viennois, C. Colinet, P. Jund, J.-C. Tédenac, Phase stability of ternary antifluorite type compounds in the quasi-binary systems Mg2X–Mg2Y (X, Y = Si, Ge, Sn) via ab-initio calculations, Intermetallics 31 (2012) 145-151.
[19] I.-H. Jung, D.-H. Kang, W.-J. Park, N.J. Kim, S. Ahn, Thermodynamic modeling of the Mg–Si–Sn system, Calphad 31(2) (2007) 192-200.
[20] M.B. Djurdjevic, Quantification of Cu Enriched Phases in Synthetic 3XX Aluminum Alloys Using the Thermal Analysis Technique, AFS Transactions 16 (2001).
[21] A.M. Samuel, F.H. Samuel, A Metallographic Study of Porosity and Fracture-Behavior in Relation to the Tensile Properties in 319.2 End-Chill Castings, Metallurgical and Materials Transactions a-Physical Metallurgy and Materials Science 26(9) (1995) 2359-2372.

[22] J.M. Tartaglia, R.E. Swartz, R.L. Bentz, J.H. Howard, Magnesium alloy ingots: Chemical and metallographic analyses, Jom 53(11) (2001) 16-19.
[23] E.G. Vajda, R.D. Bloebaum, J.G. Skedros, Validation of Energy Dispersive X-Ray Spectrometry as a Method to Standardize Backscattered Electron Images of Bone, Cells and Materials 6 (1996) 79-92.
[24] G.E. Lloyd, Atomic Number and Crystallographic Contrast Images with the SEM: A Review of Backscattered Electron Techniques, Mineralogical Magazine 51(359) (1987) 3-19.
[25] G. Neubert, S. Rogaschewski, Backscattering coefficient measurements of 15 to 60 keV electrons for solids at various angles of incidence, Physica Status Solidi (a) 59(1) (1980) 35-41.
[26] R. Wuhrer, K. Moran, Low voltage imaging and X-ray microanalysis in the SEM: challenges and opportunities, IOP Conference Series: Materials Science and Engineering 109 (2016) 012019.
[27] J.J. Friel, X-ray and Image Analysis in Electron Microscopy Princeton Gamma-Tech, Princeton, USA, 2003.
[28] R. Jenkins, Principles and practice of X-ray spectrometric analysis. Eugene P. Bertin, 2nd Edn, Plenum Press, 1975, pp. 1060. $75.00, X-Ray Spectrometry 4(4) (1975) A18-A18.
[29] D.C. Joy, C.S. Joy, Low voltage scanning electron microscopy, Micron 27(3-4) (1996) 247-263.
[30] V.M. Dusevich, J.H. Purk, J.D. Eick, Choosing the Right Accelerating Voltage for SEM (An Introduction for Beginners), Microscopy Today 18(1) (2010) 48-52.
[31] J.I. Goldstein, D.E. Newbury, J.R. Michael, N.W. Ritchie, J.H.J. Scott, D.C. Joy, Scanning electron microscopy and X-ray microanalysis, Springer2017.
[32] C.E. Lyman, D.E. Newbury, J.I. Goldstein, D.B. Williams, A.D. Romig, J.T. Armstrong, P. Echlin, C.E. Fiori, D.C. Joy, E. Lifshin, K.-R. Peters, Scanning Electron Microscopy, X-Ray Microanalysis and Analytical Electron Microscopy: A Laboratory Workbook, Plenum Press

New York, N. Y. , 1990.
[33] G.E. Lloyd, Atomic number and crystollographic content images for the SEM:a review of backscattered electron techniques, Miner Magn 51 (1987) 3-19.
[34] E.H. Darlington, Backscattering of 10-100 keV electrons from thick targets, Journal of Physics D: Applied Physics 8(1) (1975) 85.
[35] M. Kubouchi, K. Hayashi, Y. Miyazaki, Quantitative analysis of interstitial Mg in Mg2Si studied by single crystal X-ray diffraction, J. Alloys Compd. 617 (2014) 389-392.
[36] W. Liu, X. Tang, H. Li, J. Sharp, X. Zhou, C. Uher, Optimized Thermoelectric Properties of Sb-Doped Mg2(1+z)Si0.5–ySn0.5Sby through Adjustment of the Mg Content, Chem. Mater. 23(23) (2011) 5256-5263.